ChemComm

ROYAL SOCIETY OF CHEMISTRY

COMMUNICATION

View Article Online
View Journal | View Issue

Cite this: *Chem. Commun.*, 2025, **61**, 5942

Received 30th December 2024,
Accepted 17th March 2025

DOI: 10.1039/d4cc06774f

rsc.li/chemcomm

Critical impacts of metal cocatalysts on oxidation kinetics and optimal reaction conditions of photocatalytic methane reforming†

Hiromasa Sato, [a] Hikaru Saito, [a] Taisuke Higashi[a] and Toshiki Sugimoto *[ab]

Metal cocatalysts in photocatalysis are typically regarded as promoting only the reduction reactions. Here, we demonstrate that photocatalytic oxidation kinetics and optimal pressure of methane vary significantly with the loading amount of metal cocatalysts. These variations are well described by kinetic analyses treating molecular-level congestion of oxidation intermediates.

Photocatalysis represents a promising approach for driving redox reactions using light, surpassing thermodynamic limitations.[1–6] Most advanced photocatalyst systems rely on noble metal cocatalysts to achieve high photocatalytic activity.[7,8] Indeed, numerous studies have demonstrated that the incorporation of metal cocatalysts significantly improves the activity of semiconductor-based photocatalysts.[9,10] Conventionally, it has been widely accepted that the metal cocatalysts act mostly as sinks of photogenerated electrons (e^-) and serve exclusively as reduction sites.[7,8]

Some previous studies offered new insights into the role of metal cocatalysts in photocatalysis. For instance, previous density functional theory calculations[11] and infrared spectroscopy[12] have suggested that holes (h^+) generated through band-gap excitation of semiconductor photocatalysts can be trapped by metal cocatalysts. This hypothesis is based on the simple assumption that h^+-accumulating metal cocatalysts act as recombination centers for photogenerated e^- and h^+, without investigating the actual photocatalytic performance. By contrast, our recent study combining *operando* spectroscopy with real-time mass spectrometry demonstrated that e^- and h^+ can be separately captured by different metal cocatalysts, and the metal cocatalysts play key roles not only in promoting reduction reactions but also in accelerating oxidation reactions, while minimizing charge recombination.[13] Furthermore, metal cocatalysts not only enhance overall photocatalytic activity but also influence the oxidation selectivity.[13] These recent findings highlight the need for a deeper understanding of the microscopic roles of metal cocatalysts, beyond the conventional view that they merely promote reduction reactions by accumulating only photogenerated e^-.[7,8]

In this study, we provide further experimental evidence that metal cocatalysts directly impact the photocatalytic oxidation processes. The oxidation process is recognized as the rate-determining step of photocatalysis,[14–16] and the oxidation kinetics should be affected by modulation of this step. To examine whether variations in metal cocatalysts alter the dynamics and kinetics of the rate-determining oxidation step, we investigated the effects of loading amounts of metal cocatalysts on photocatalytic methane conversion with water. Methane is the main component of natural gas and a ubiquitous natural resource. Due to its robust C–H bonds, achieving methane conversion under ambient temperatures and pressures poses a significant challenge in advancing sustainable technologies.[17] Conventional thermocatalytic methane conversion requires harsh conditions (>1000 K and >20 atm);[18] in contrast, photocatalysis offers a more sustainable approach by enabling methane activation and oxidation under ambient conditions (~ 300 K and ~ 1 atm).[17] Herein, we focused on the Pt- or Pd-loaded gallium oxide (Ga_2O_3) particles as robust model systems for photocatalytic methane reforming.[13,15,19] Through controlled experiments under varying methane pressures (P_{CH_4}), we observed that the amount of metal cocatalysts significantly influences the P_{CH_4} dependence of the photocatalytic performance, resulting in pronounced modulation of the optimal P_{CH_4} conditions below ambient pressures. This variation suggests that the loading of metal cocatalysts affects the congestion of intermediate species involved in methane oxidation processes. These results highlight the crucial role of metal cocatalysts as active sites also for the oxidation reaction.

β-Ga_2O_3 is a well-known d^{10} photocatalyst[2] with stable activity and robustness.[20] The four β-Ga_2O_3 samples containing either 0.01 wt% or 1 wt% of metal Pt or Pd cocatalysts (Pt(0.01 wt%)/Ga_2O_3, Pd(0.01 wt%)/Ga_2O_3, Pt(1 wt%)/Ga_2O_3, Pd(1 wt%)/Ga_2O_3) were prepared by the impregnation method (see Note S1-1, ESI,† for details). As described in detail in Note S1-2 (ESI†), the photocatalytic performance of these metal-loaded Ga_2O_3 samples was evaluated by irradiating a deep

[a] *Department of Materials Molecular Science, Institute for Molecular Science, Okazaki, Aichi 444-8585, Japan. E-mail: toshiki-sugimoto@ims.ac.jp*
[b] *Graduate Institute for Advanced Studies (SOKENDAI), Okazaki, Aichi 444-8585, Japan*

† Electronic supplementary information (ESI) available. See DOI: https://doi.org/10.1039/d4cc06774f

ultraviolet (UV) lamp (~90 mW cm^{-2} at 260 ± 15 nm) at various P_{CH_4} under a fixed water vapor pressure (P_{H_2O}) of 2 kPa. Notably, the photocatalytic activity under LED light irradiation at 390 nm was low, although loading the Pt and Pd cocatalysts enhanced the light absorption in this wavelength region (Fig. S1-5, ESI†).[13] This indicates that e^- and h^+ species generated by the excitation of the metal cocatalysts[21] have little contribution, whereas those generated by the band-gap excitation of Ga_2O_3 dominantly induce photocatalytic methane conversion.[13] Under the irradiation of a deep UV lamp, the sample temperature was ~318 K and a single layer of adsorbed water molecules covered the sample surfaces at P_{H_2O} = 2 kPa (~20% relative humidity for 318 K samples)[22–24] as described in Note S1-3 (ESI†).

Fig. 1 illustrates the P_{CH_4} dependence of the formation rates of H_2 (R_{H_2}) and CO_2 (R_{CO_2}) for the four photocatalyst samples. The rate of H_2 evolution was approximately four times higher than that of CO_2 formation ($R_{CO_2} \approx 0.25R_{H_2}$), indicating nearly stoichiometric CO_2 production in the steam methane reforming reaction ($CH_4 + 2H_2O \rightarrow CO_2 + 4H_2$). In addition, C_2H_6 derived from the side reaction ($2CH_4 \rightarrow C_2H_6 + H_2$)[25] was also detected, as will be discussed later (Fig. 3).

As reported previously for the Pt(1 wt%)/Ga_2O_3 and Pd(1 wt%)/Ga_2O_3 photocatalysts,[13,15] R_{H_2} and R_{CO_2} showed a strong dependence on P_{CH_4}; the rates increased sharply with P_{CH_4} below ~30 kPa (0.3 atm) and nearly reached saturation value at ~100 kPa (1 atm). In contrast, we found that the P_{CH_4} profiles for the Pt(0.01 wt%)/Ga_2O_3 and Pd(0.01 wt%)/Ga_2O_3 photocatalysts differ markedly from those for the 1 wt% metal-loaded samples (Fig. 1b); while R_{H_2} and R_{CO_2} increased with P_{CH_4} below ~20 kPa, they began to decline at P_{CH_4} above ~20 kPa. Thus, for the 1 wt% metal-loaded samples, the photocatalytic performance for methane conversion is almost maximized at ambient pressure (~1 atm), whereas the optimal P_{CH_4} is around 20 kPa, well below 1 atm, for the 0.01 wt% metal-loaded samples. The observed variation in the P_{CH_4} profile (Fig. 1) indicates that the microscopic redox reaction kinetics of photocatalytic steam methane reforming is affected by the loading amount of metal cocatalysts. Beyond the conventional assumption that the role of metal cocatalysts is limited solely to reduction reactions in the semiconductor bandgap photoexcitation scheme,[7,8] our experimental results clearly show the impact of metal cocatalysts not only on reduction (H_2 evolution) but also on oxidation (CO_2 formation) processes in this widely used photoexcitation scheme.

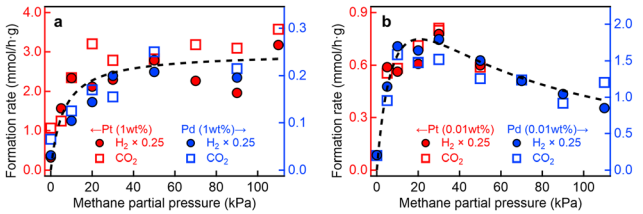

Fig. 1 P_{CH_4} profiles of photocatalytic steam methane reforming. Formation rates of H_2 and CO_2 for (a) Pt(1 wt%)/and Pd(1 wt%)/Ga_2O_3 photocatalysts, and (b) Pt(0.01 wt%)/and Pd(0.01 wt%)/Ga_2O_3 photocatalysts under UV irradiation as a function of P_{CH_4} at P_{H_2O} = 2 kPa. Curve fitting results based on eqn (3) with U = 40 kJ mol^{-1} and eqn (4) with U = 37 kJ mol^{-1} are also shown in (a) and (b), respectively.

To provide microscopic insights on the influence of metal cocatalyst loadings on the reaction kinetics, detailed analysis was carried out on the observed P_{CH_4} dependence of the photocatalytic performance (Fig. 1). In general, the CH_4 oxidation process toward CO_2 can be divided into three steps (Fig. 2a and b):[13,15] (i) dissociative adsorption and desorption of CH_4 at vacant active sites, (ii) sequential reactions involving surface intermediate species,[26] and (iii) desorption of the final products, primarily CO_2 (see also Note S2, ESI†). The C–H cleavage of CH_4 in the first step is initiated by hydrogen abstraction from photoactivated interfacial water species,[15] resulting in the formation of activated methane species (X_1 = $^\bullet CH_3$) that subsequently chemisorb onto the catalyst surfaces (Fig. 2a and b). This process leads to the P_{CH_4} dependence of the coverage of $^\bullet CH_3$ (θ_{CH_3}) similar to the Langmuir adsorption isotherm as follows:[13,15]

$$\theta_{CH_3} = KP_{CH_4}/(1 + KP_{CH_4}), \quad (1)$$

where K is the equilibrium constant for the first step (dissociative adsorption of methane and desorption of methyl radical; $CH_{4(gas)} + {}^\bullet OH_{(ad)} \leftrightarrow {}^\bullet CH_{3(ad)} + H_2O_{(ad)}$), expressed as $K \equiv k_{ad}/k_{de} \propto \exp(U/k_BT_s)$. Here, k_B and T_s represent the Boltzmann constant and surface temperature, respectively, and U denotes the stabilization energy of the $^\bullet CH_{3(ad)}$ intermediate (see Note S2-1 for details of the kinetic analysis, ESI†).

Notably, the product yields linearly increased with irradiation time,[13,15] indicating that the reactions proceeded under steady-state conditions. In the case where the reaction of adsorbed $^\bullet CH_3$ is rate-determining,[13,15] R_{CO_2} under steady-state conditions is dominated by the reaction of $^\bullet CH_3$ as follows:

$$R_{CO_2} \approx k_1'\theta_{CH_3}\theta_v, \quad (2)$$

where k_1' is the rate constant factor for the rate-determining reaction process, and $\theta_v \equiv 1 - \sum\theta_{X_i}$ (θ_{X_i} is the coverage of the i-th intermediate species (i = 1, 2,...,8, see Fig. 2a and b) that block the reaction sites) represents the fraction of vacant surface sites available for the forward reaction of $^\bullet CH_3$ species toward CO_2 (see also Note S2 for details, ESI†). When the density of surface reaction sites is high enough that few active sites are occupied ($\theta_v \approx 1$) in steady reaction

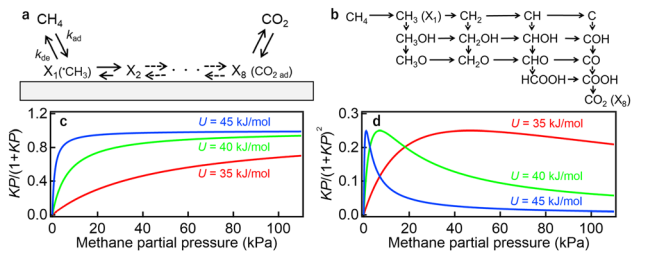

Fig. 2 Reaction scheme and kinetic analysis of photocatalytic steam methane reforming. (a) Surface reaction pathway for the conversion of CH_4 to CO_2, where X_i (i = 1, 2,...,8) represents reaction intermediates; specifically, X_1 and X_8 denote methyl radical ($^\bullet CH_3$) and adsorbed CO_2, respectively. For simplicity, the contribution of OH radical species ($^\bullet OH$) generated *via* water oxidation ($H_2O + h^+ \rightarrow {}^\bullet OH + h^+$)[15] is omitted in the diagram. (b) Possible reaction intermediate species from CH_4 to CO_2 in Fig. 2a through hydrogen abstraction or hydroxylation by photoactivated water species.[26] (c) and (d) P_{CH_4} dependence of R_{CO_2} given by (c) eqn (3) and (d) eqn (4) at different values of U (35, 40, and 45 kJ mol^{-1}).

conditions, eqn (2) is approximated as

$$R_{CO_2} \approx k'_1\theta_{CH_3} = k'\left(KP_{CH_4}/\left(1+KP_{CH_4}\right)\right). \quad (3)$$

The P_{CH_4} profiles of R_{CO_2} at typical values of U are displayed in Fig. 2c. As U increases, the reaction activity tends to start increasing at the lower P_{CH_4}. Then, with increasing P_{CH_4}, reaction activity monotonically increases as an upward convex curve and then saturates in response to the abundance of the rate-determining intermediate species.

In contrast, when the density of active sites is not sufficiently high, the coverage of intermediate species competitively affects the fraction of vacant surface sites. Since the majority of the surface intermediates are $^{\bullet}CH_3$ ($\sum\theta_{X_i} \approx \theta_{CH_3}$) in the case where the reaction of adsorbed $^{\bullet}CH_3$ intermediates is rate-determining,[13,15] the fraction of vacant sites is approximated as $\theta_v \approx 1 - \theta_{CH_3}$, yielding the following form of eqn (2):

$$R_{CO_2} \approx k'_1\theta_{CH_3}\left(1-\theta_{CH_3}\right) = k'_1\left(KP_{CH_4}/\left(1+KP_{CH_4}\right)^2\right). \quad (4)$$

In this case, although the reaction activity starts to increase at the lower P_{CH_4} region, it begins to decrease with increasing P_{CH_4} after reaching a maximum value (Fig. 2d). This characteristic P_{CH_4} profile arises from a balance between two competing effects (Fig. S2-3, ESI†): the positive impact of increasing the abundance of the rate-determining intermediate species and the negative impact of molecular-level congestion due to the reduced availability of vacant active sites for further reactions of the rate-determining intermediate species ($X_1 \rightarrow X_2$ in Fig. 2a and b). It should also be noted that, even if the rate-determining step is not the forward reaction of $^{\bullet}CH_3$ (X_1) but rather another surface reaction involving different intermediate species ($X_i \rightarrow X_{i+1}$ in Fig. 2a and b), the P_{CH_4} dependencies similar to eqn (3) and (4) are derived as discussed in Note S3 (ESI†).

For the Pt(1 wt%)/Ga_2O_3 and Pd(1 wt%)/Ga_2O_3 photocatalysts, P_{CH_4} profiles of R_{CO_2} were well-fitted to eqn (3) with a stabilization energy U of 40 kJ mol^{-1} (Fig. 1a), as reported in our previous studies.[13,15] On the other hand, the reaction activity for the Pt(0.01 wt%)/Ga_2O_3 and Pd(0.01 wt%)/Ga_2O_3 photocatalysts behaved differently, showing a better fit to eqn (4) compared to eqn (3) with a similar U value of 37 kJ mol^{-1} (Fig. 1b). These curve-fitting analyses indicate that a sufficient number of active sites are provided for the 1 wt% loading of metal cocatalysts, avoiding competitive occupation of active sites by intermediate species. In contrast, the 0.01 wt% loading provides a limited number of active sites for intermediate species, resulting in the competition of positive and negative effects of active site occupation by intermediate species. Therefore, the observed modulation of reaction kinetics upon loading amount of metal cocatalysts provides compelling evidence that the metal cocatalysts themselves function as reaction fields for the photocatalytic oxidation.[13] These results further suggest that the photogenerated e^- and h^+ migrate separately from Ga_2O_3 to the metal cocatalyst particles,[13] enabling certain metal cocatalysts to act as reduction sites by capturing electrons, while others function as oxidation sites by trapping holes, as discussed in detail in Note S4 (ESI†).

Additional important evidence supporting that metal cocatalysts are deeply involved in molecular-level dynamics and congestion of photocatalytic oxidation processes has been obtained. This is demonstrated by focusing on the simultaneously induced side-reaction of methane into ethane ($2CH_4 \rightarrow C_2H_6 + H_2$). Fig. 3 illustrates the P_{CH_4} dependence of ethane formation rates ($R_{C_2H_6}$) for the four photocatalyst samples. In contrast to R_{CO_2} (Fig. 1), the P_{CH_4} profiles of $R_{C_2H_6}$ not only vary depending on the loading amount of metal cocatalysts but also vary depending on the metal element of cocatalysts (Fig. 3). As detailed in our previous study,[13] the P_{CH_4} profiles for the Pt(1 wt%)/Ga_2O_3 and Pd(1 wt%)/Ga_2O_3 photocatalysts (Fig. 3a) were described by the second-order and first-order reactions of the surface adsorbed $^{\bullet}CH_3$ intermediate species, respectively, as follows:

$$R_{C_2H_6}(\text{Pt 1 wt\%}) \approx k''_1{\theta_{CH_3}}^2 = k''_1\left(\left(KP_{CH_4}\right)^2/\left(1+KP_{CH_4}\right)^2\right), \quad (5)$$

$$R_{C_2H_6}(\text{Pd 1 wt\%}) \approx k''_1\theta_{CH_3} = k''_1\left(KP_{CH_4}/\left(1+KP_{CH_4}\right)\right), \quad (6)$$

where k''_1 is a rate constant. The apparent difference of the reaction order indicates that the coupling of $^{\bullet}CH_3$ intermediates ($2^{\bullet}CH_3 \rightarrow C_2H_6$) occurs on the catalyst surfaces (eqn (5) and Fig. S5-1a, S5-2, ESI†) for the Pt(1 wt%)/Ga_2O_3, while it proceeds in the gas phase for the Pd(1 wt%)/Ga_2O_3 (eqn (6) and Fig. S5-1b, S5-5, ESI†).[13]

As the main reaction ($CH_4 + 2H_2O \rightarrow CO_2 + 4H_2$), we found that the limited 0.01 wt% loading of metal cocatalysts also has a significant impact on the P_{CH_4} profiles of $R_{C_2H_6}$ (Fig. 3b). For the Pt(0.01 wt%)/Ga_2O_3 photocatalyst, $R_{C_2H_6}$ steeply declined at $P_{CH_4} > 10$ kPa after the initial increase at $P_{CH_4} < 10$ kPa. A similar trend was observed for the Pd(0.01 wt%)/Ga_2O_3 photocatalyst, although the decline was more gradual compared to the Pt(0.01 wt%)/Ga_2O_3 photocatalyst. These non-monotonic P_{CH_4} profiles are derived from the competition between the positive impact of increasing the abundance of the rate-determining $^{\bullet}CH_3$ intermediate species and the negative impact of their molecular-level congestion due to the reduced availability of vacant active sites for further reactions. Then, these observed P_{CH_4} profiles were well-fitted with the following equations explicitly incorporating the effect of competing occupation

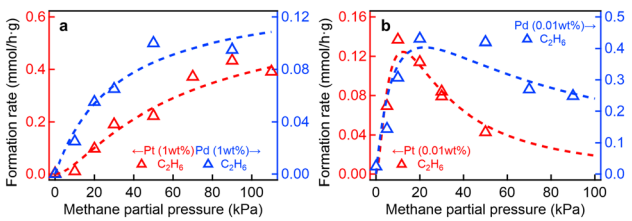

Fig. 3 P_{CH_4} profiles of photocatalytic ethane formation from methane. Formation rates of C_2H_6 for (a) Pt(1 wt%)/and Pd(1 wt%)/Ga_2O_3 photocatalysts, and (b) Pt(0.01 wt%)/and Pd(0.01 wt%)/Ga_2O_3 photocatalysts under UV irradiation at P_{H_2O} = 2 kPa. Curve fitting results based on eqn (5) and (6) with U = 36 kJ mol^{-1}, eqn (7) with U = 39 kJ mol^{-1}, and eqn (8) with U = 37 kJ mol^{-1} are also shown in (a) and (b).

of limited active sites by intermediate species ($\theta_v \approx 1 - \theta_{CH_3}$).

$$R_{C_2H_6}(\text{Pt } 0.01\text{ wt\%}) \approx k_1''(\theta_{CH_3}\theta_v)^2 = k_1''(\theta_{CH_3}(1-\theta_{CH_3}))^2 = k_1''\left((KP_{CH_4})^2/(1+KP_{CH_4})^4\right), \quad (7)$$

$$R_{C_2H_6}(\text{Pd } 0.01\text{ wt\%}) \approx k_1''(\theta_{CH_3}\theta_v) = k_1''\theta_{CH_3}(1-\theta_{CH_3}) = k_1''\left(KP_{CH_4}/(1+KP_{CH_4})^2\right). \quad (8)$$

The decline of $R_{C_2H_6}$ is more significant for eqn (7) than eqn (8) (Fig. S5-7b, ESI†). As described in detail in Note S5 (ESI†), the apparent difference of the reaction order for $\theta_{CH_3}\theta_v$ indicates that the homocoupling of methyl radical intermediates ($2^{\bullet}CH_3 \rightarrow C_2H_6$) occurs on the catalyst surfaces (eqn (7) and Fig. S5-1a, S5-3, ESI†) for the Pt(0.01 wt%)/Ga_2O_3 sample, while it proceeds in the gas phase for the Pd(0.01 wt%)/Ga_2O_3 sample (eqn (8) and Fig. S5-1b, S5-6, ESI†).[13] Even though the homocoupling of $^{\bullet}CH_3$ proceeds in the gas phase for the Pd(0.01 wt%)/Ga_2O_3 sample (Fig. S5-1b, ESI†), manifestation of the negative P_{CH_4} impact in the apparent first order reaction suggests that the desorption of $^{\bullet}CH_3$ into the gas phase occurs after it migrates from its initial adsorption site to a nearby vacant site that is more preferable for desorption (see Fig. S5-4, ESI† for more precise picture). Note that, in the situation where the competitive occupation of active sites by intermediate species is negligible ($\theta_v \approx 1$), eqn (7) and (8) correspond to eqn (5) and (6), respectively. Thus, our results clearly demonstrate that the competitive occupation of active surface sites by reaction intermediates and the resulting modulation of reaction kinetics emerges also in the side reaction pathway of methane partial oxidation ($CH_4 \rightarrow {}^{\bullet}CH_3 \rightarrow C_2H_6$). Owing to this effect, the optimal P_{CH_4} condition for the photocatalytic ethane formation also significantly varied with the amount of metal loading (Fig. 3a and b). Therefore, the observed modulation of ethane formation kinetics also provides compelling evidence that the metal cocatalysts themselves functions as active sites for oxidative photoactivation. Furthermore, the homocoupling pathway for ethane formation is independent of the loading amount of metal cocatalysts (1 wt% or 0.01 wt%) but varies with the elements of metal cocatalysts used (Pt or Pd). This is also a manifestation of the phenomena that the metal cocatalysts fundamentally influence oxidation kinetics and dynamics.

Finally, we emphasize that our concept of metal cocatalysts also provides a rationale for previously reported, yet incomprehensible, results in photocatalytic oxidation. For instance, variations in the activity of photocatalytic oxidation have been reported for semiconductor photocatalysts loaded with metal cocatalysts of different elements and/or loading amount.[27–29] Nevertheless, metal cocatalysts have traditionally been regarded solely as the trapping site of e^- and the resultant promotors of reduction reactions.[7,8] This interpretation arises from the seemingly plausible assumption that more efficient oxidation reactions are simply driven by an increased number of h^+ that avoid annihilative charge recombination with e^- due to the preferential trapping/consumption of e^- facilitated by metal cocatalysts.[11,12] Beyond this classical picture, our results provide a series of solid evidence that the metal cocatalyst actively takes part in photocatalytic oxidation and modulates oxidation kinetics/dynamics, shedding new light on the complex interplay between cocatalyst loading and interfacial reaction.

This work was supported by JSPS KAKENHI [JP22H00296, JP24H02205, JP22KJ1427, JP22KJ3098], JST CREST [JPMJCR22L2], JST ACT-X [JPMJAX24D7] and Demonstration Project of Innovative Catalyst Technology for Decarbonization through Regional Resource Recycling, the Ministry of the Environment, Government of Japan.

Data availability

The data and analytical details supporting this article have been included as part of the ESI.†

Conflicts of interest

There are no conflicts to declare.

Notes and references

1 A. L. Linsebigler, G. Lu and J. T. Yates, *Chem. Rev.*, 1995, **95**, 735.
2 A. Kudo and Y. Miseki, *Chem. Soc. Rev.*, 2009, **38**, 253.
3 P. Zhang and X. W. D. Lou, *Adv. Mater.*, 2019, **31**, 1900281.
4 K. Villa and M. Pumera, *Chem. Soc. Rev.*, 2019, **48**, 4966.
5 Q. Wang and K. Domen, *Chem. Rev.*, 2020, **120**, 919.
6 M. Yamauchi, H. Saito, T. Sugimoto, S. Mori and S. Saito, *Coord. Chem. Rev.*, 2022, **472**, 214773.
7 J. Yang, D. Wang, H. Han and C. Li, *Acc. Chem. Res.*, 2013, **46**, 1900.
8 J. Ran, J. Zhang, J. Yu, M. Jaroniec and S. Z. Qiao, *Chem. Soc. Rev.*, 2014, **43**, 7787.
9 R. Su, R. Tiruvalam, A. J. Logsdail, Q. He, C. A. Downing, M. T. Jensen, N. Dimitratos, L. Kesavan, P. P. Wells, R. Bechstein, H. H. Jensen, S. Wendt, C. R. A. Catlow, C. J. Kiely, G. J. Hutchings and F. Besenbacher, *ACS Nano*, 2014, **8**, 3490.
10 T. Kotani, K. Ogawa, H. Suzuki, K. Kato, O. Tomita, A. Yamakata and R. Abe, *EES Catal.*, 2023, **1**, 255.
11 C. L. Muhich, Y. Zhou, A. M. Holder, A. W. Weimer and C. B. Musgrave, *J. Phys. Chem. C*, 2012, **116**, 10138.
12 M. Yoshida, A. Yamakata, K. Takanabe, J. Kubota, M. Osawa and K. Domen, *J. Am. Chem. Soc.*, 2009, **131**, 13218.
13 H. Saito, H. Sato, T. Higashi and T. Sugimoto, *Angew. Chem., Int. Ed.*, 2023, **62**, e202306058.
14 X. Ma, Y. Shi, J. Liu, X. Li, X. Cui, S. Tan, J. Zhao and B. Wang, *J. Am. Chem. Soc.*, 2022, **144**, 13565.
15 H. Sato, A. Ishikawa, H. Saito, T. Higashi, K. Takeyasu and T. Sugimoto, *Commun. Chem.*, 2023, **6**, 8.
16 H. Zou, Y. Qi, S. Du, Y. Bao, X. Xin, W. Fan, Y. Xiao, S. Jin, Z. Feng and F. Zhang, *J. Am. Chem. Soc.*, 2024, **146**, 28182.
17 X. Meng, X. Cui, N. P. Rajan, L. Yu, D. Deng and X. Bao, *Chem*, 2019, **5**, 2296.
18 A. I. Olivos-Suarez, À. Szécsényi, E. J. M. Hensen, J. Ruiz-Martinez, E. A. Pidko and J. Gascon, *ACS Catal.*, 2016, **6**, 2965.
19 H. Sato and T. Sugimoto, *J. Am. Chem. Soc.*, 2024, **146**, 24800.
20 F. Amano, C. Akamoto, M. Ishimaru, S. Inagaki and H. Yoshida, *Chem. Commun.*, 2020, **56**, 6348.
21 S. Luo, X. Ren, H. Lin, H. Song and J. Ye, *Chem. Sci.*, 2021, **12**, 5701.
22 K. Shirai, T. Sugimoto, K. Watanabe, M. Haruta, H. Kurata and Y. Matsumoto, *Nano Lett.*, 2016, **16**, 1323.
23 Z. Lin, H. Saito, H. Sato and T. Sugimoto, *J. Am. Chem. Soc.*, 2024, **146**, 22276.
24 F. Amano, A. Ishikawa, H. Sato, C. Akamoto, S. P. Singh, S. Yamazoe and T. Sugimoto, *Catal. Today*, 2024, **426**, 114375.
25 G. Wang, X. Mu, J. Li, Q. Zhan, Y. Qian, X. Mu and L. Li, *Angew. Chem., Int. Ed.*, 2021, **60**, 20760.
26 V. S. Bagotzky, Y. B. Vassiliev and O. A. Khazova, *J. Electroanal. Chem.*, 1977, **81**, 229.
27 H. Yuzawa, S. Yoneyama, A. Yamamoto, M. Aoki, K. Otake, H. Itoh and H. Yoshida, *Catal. Sci. Technol.*, 2013, **3**, 1739.
28 Y. Negishi, Y. Matsuura, R. Tomizawa, W. Kurashige, Y. Niihori, T. Takayama, A. Iwase and A. Kudo, *J. Phys. Chem. C*, 2015, **119**, 11224.
29 S. Mori and S. Saito, *Green Chem.*, 2021, **12**, 810.